THE ASTROPHYSICAL JOURNAL, 435:852–863, 1994 November 10

MOLECULAR ROTATIONAL LINE PROFILES FROM OXYGEN-RICH RED GIANT WINDS

K. JUSTTANONT,[1,2,3] C. J. SKINNER,[4,5] AND A. G. G. M. TIELENS[1]

Received 1993 June 1; accepted 1994 February 10

ABSTRACT

We have developed a radiative transfer model of the dust and gas envelopes around late-type stars. The gas kinetic temperature for each star is calculated by solving equations of motion and the energy balance simultaneously. The main processes include viscous heating and adiabatic and radiative cooling. Heating is dominated by viscosity as the grains stream outward through the gas, with some contribution in oxygen-rich stars by near-IR pumping of H_2O followed by collisional de-excitation in the inner envelope. For O-rich stars, rotational H_2O cooling is a dominant mechanism in the middle part of the envelope, with CO cooling being less significant. We have applied our model to three well-studied oxygen-rich red giant stars. The three stars cover a wide range of mass-loss rates, and hence they have different temperature structures. The derived temperature structures are used in calculating CO line profiles for these objects. Comparison of the dust and gas mass-loss rates suggests that mass-loss rates are not constant during the asymptotic giant branch phase. In particular, the results show that the low CO 1–0 antenna temperatures of OH/IR stars reflect an earlier phase of much lower mass-loss rate.

Subject headings: circumstellar matter — line: profiles — molecular processes — stars: giants — stars: mass loss

1. INTRODUCTION

CO has been detected in a number of late-type stars (e.g., Knapp et al. 1982; Knapp & Morris 1985; Heske et al. 1990) in the $v = 0$, $J = 1$–0, and 2–1 rotational transitions. These observations have commonly been used to determine the gas mass-loss rate from red giants. The structure of the molecule is well studied, hence the line transfer process can be accurately calculated. Moreover, the abundance of CO in the outflow is appreciable, thereby making it an extremely useful tool to probe the mass-loss rates of late type stars. However, the interpretation of observed CO antenna temperatures in terms of mass-loss rates is not straightfoward. In particular, such a quantitative analysis requires knowledge of the gas kinetic temperature of the envelope, which is poorly known observationally or theoretically. Interpretation of CO 1–0 observations of extreme OH/IR stars—those with $\dot{M} \sim 10^{-4}\ M_\odot\ \mathrm{yr}^{-1}$—is particularly unclear. Such objects show much lower CO 1–0 antenna temperature than expected from simple considerations (Heske et al. 1990). This has been interpreted as either spatial variation in excitation condition (i.e., $T_{ex} < T_g$), or temporal variation in the mass-loss rate.

Many authors have considered the temperature structure of late-type stars but have generally concentrated on C-rich objects, in which CO is the molecule mainly responsible for the radiative cooling. However, for O-rich stars, H_2O, which has an extremely complicated vibrational and rotational spectrum, is abundant and is much more efficient in cooling than CO. Goldreich & Scoville (1976, hereafter GS) calculated the energy balance for IRC +10011 and showed that its temperature structure does not behave as a simple power law.

We have developed a theoretical model for the gas kinetic temperature of circumstellar envelopes, taking the main heating and cooling processes into account. We calculate temperature structures in O-rich stars by solving the equations of motion of the gas and the energy balance simultaneously, since the temperature structure is coupled to the velocity structure through the escape of photons and through adiabatic cooling. This temperature structure is then used in an accurate CO radiation transfer code.

In § 2, we discuss the processes which result in the final gas kinetic temperature in O-rich stars. The results are reported in § 3 for three stars, with different mass-loss rates. Their CO line profiles are modeled in § 4.

2. GAS KINETIC TEMPERATURE CALCULATION FOR O-RICH STARS

In order to obtain the gas kinetic temperature of a circumstellar envelope, the equations of motion and energy balance must be solved simultaneously. Below we discuss the calculations and assumptions. In our model, we have included a grain size distribution.

2.1. *The Gas and Dust Velocity*

The main assumptions in the calculation are that the mass loss is spherically symmetric and constant. It is also assumed that the outflow is driven by radiation pressure on the dust which forms at the radius where the dust temperature falls below its condensation temperature (1000 K for silicate). Since the absorption cross sections of dust grains are much larger than those for gas molecules, the dust gains more momentum and is driven outward, with the gas being dragged along with it. Collisions of gas molecules with the drifting dust grains transfer momentum. The frequent collisions among gas molecules redistribute this momentum rapidly to all gas. Dust and gas are then said to be momentum coupled (Gilman 1972). The

[1] NASA/Ames Research Center, MS245-3, Moffett Field, CA 94035.
[2] Department of Physics and Astronomy, University College London, Gower Street, London WC1E 6BT, Great Britain.
[3] Institut d'Astrophysique, 98 bis Boulevard Arago, 75014 Paris, France.
[4] Institute of Geophysics and Planetary Physics, L-413, Lawrence Livermore National Laboratory, P.O. Box 808, Livermore, CA 94581-9900.
[5] Nuffield Radio Astronomy Laboratory, Jodrell Bank, Macclesfield, Cheshire, SK11 9DL, Great Britain.

equation of motion of the gas is given by (see Tielens 1983)

$$v\frac{dv}{dr} = (\Gamma - 1)\frac{GM_*}{r^2}, \quad (1)$$

where v is the gas velocity, M_* is the stellar mass, r is the radial distance from the star, and Γ is defined as the ratio of the radiation pressure force on the dust to the gravitational force on the gas. Adopting a grain size distribution by number, $n_d(a)$, and radiation pressure efficiency, $Q(a, \lambda)$, the expression for Γ can be written as

$$\Gamma = \int\int \frac{\sigma_d Q(a, \lambda)L(\lambda)}{4\pi cGM_*}\frac{n_d(a)}{\rho}\, d\lambda\, da, \quad (2)$$

where σ_d is the geometric cross section of the dust, $L(\lambda)$ is the stellar luminosity at wavelength λ, and ρ is the gas density. Here, for O-rich stars, silicate optical constants derived from the observed energy distributions in the work by Justtanont & Tielens (1992) have been adopted to calculate the radiation pressure efficiencies. The total dust mass-loss rate can be written as the integral of the dust mass-loss rate for each grain size, $\dot{M}(a)$

$$\dot{M}_d = \int \dot{M}(a)da = \int n_d(a)\tfrac{3}{4}\pi a^3\rho_s 4\pi r^2(v + v_{\rm drift})da, \quad (3)$$

where $n_d(a)$ is given by the standard interstellar grain size distribution ($= Aa^{-3.5}n_{\rm H}$, with A being a constant and $n_{\rm H}$ being the hydrogen number density [Mathis, Rumpl, & Nordsieck 1977, hereafter MRN]); ρ_s is the specific density of the dust; and $v_{\rm drift}$ is the drift velocity of dust grains through the gas. Hence,

$$\dot{M}_d = \int Aa^{-3.5}n_{\rm H}\tfrac{4}{3}\pi a^3\rho_s 4\pi r^2(v + v_{\rm drift})da. \quad (4)$$

The drift velocity of a grain of size a can be calculated by equating the radiation pressure force with the gas drag force. This leads to

$$v^2_{\rm drift}(a) = \frac{1}{2}\left[\left\{\left[\frac{2v}{\dot{M}c}\int Q(a, \lambda)L(\lambda)d\lambda\right]^2 + c_s^4\right\}^{0.5} - c_s^2\right], \quad (5)$$

where c_s is the local sound speed. In the limit where c_s is small compared to the outflow speed, this expression is reduced to

$$v^2_{\rm drift}(a) = \int \frac{Q(a, \lambda)L(\lambda)v}{\dot{M}c}\, d\lambda. \quad (6)$$

We note that for grains with radius smaller than the wavelength, $Q \propto a$; hence, $v_{\rm drift} \propto a^{0.5}$. The factor Γ can be written as

$$\Gamma = \int\int \frac{\pi a^2 Q(a, \lambda)L(\lambda)}{4\pi cGM_*}\frac{\dot{M}(a)}{(4/3)a^3\rho_s 4\pi r^2(v + v_{\rm drift})}\frac{4\pi r^2 v}{\dot{M}}\, d\lambda\, da = \frac{3v}{16\pi\rho_s cGM_*\dot{M}}\int\int \frac{Q(\lambda, a)L(\lambda)\dot{M}(a)}{a(v + v_{\rm drift})}\, d\lambda\, da, \quad (7)$$

where $\dot{M}$ refers to the gas mass-loss rate; $\dot{M} = 4\pi r^2\rho v$ for $\dot{M}$ and v constant in time. The numerical procedure used here is as follows. At the inner radius, where dust condenses out (r_i), the gas is assumed to flow with the local sound velocity at the gas temperature, T (≈ 1000 K). Then, adopting a value for the dust mass-loss rate, for example, determined from analysis of infrared observations, and assuming a dust-to-gas ratio, $\delta = \dot{M}_d/\dot{M}$, the drift velocities and Γ can be calculated from equations (6) and (7), respectively. The momentum equation (1) can then be integrated numerically to calculate the gas velocity as a function of radius. The only other free parameter in this scheme is the dust-to-gas mass ratio. In our detailed studies of red giants, the parameter δ is varied until the calculated terminal velocity of the gas agrees with the observed value. Finally, the gas and dust density distributions follow from the equations of continuity and the derived velocity laws. In general, the density will follow a r^{-2} law in the outer portion of the outflow, but will vary more rapidly in the inner region (Schutte & Tielens 1989).

2.2. *The Gas Kinetic Temperature*

In order to calculate the gas kinetic temperature as a function of radius, all the major heat sources and sinks must be considered. Here, we include heating by collision between dust and gas, radiative heating and cooling by molecules present in the outflow and the adiabatic expansion.

2.2.1. *Gas-Grain Collisional Heating*

The main heating in the circumstellar envelope is due to collisions between gas and dust grains. The viscous heat input per unit volume due to a grain of radius a is

$$H = \tfrac{1}{2}m_{\rm H_2}n_{\rm H_2}v^3_{\rm drift}(a)n_d(a)\pi a^2. \quad (8)$$

Each grain size contributes differently to the heating rate. Although bigger grains have larger radiation pressure efficiencies, there are fewer of them in the outflow due to the $a^{-3.5}$ law. The heating rate can be seen to depend on the mass-loss rate and velocity of the outflow. A higher mass-loss rate and larger outflow velocity result in a higher heating rate, i.e., $H \propto n_{\rm H_2}n_d v^3_{\rm drift} \propto \dot{M}^2 v^3_{\rm drift}$, and from equation (6), $H \propto \dot{M}^{0.5}v^{1.5}$. The final expression for the heating rate can be written as

$$H = \tfrac{1}{2}m_{\rm H_2}n_{\rm H_2}(1 + f/2)\pi\int a^2 n_d(a)v^3_{\rm drift}(a)da = \tfrac{1}{2}m_{\rm H_2}n_{\rm H_2}(1 + f/2)\pi An_{\rm H}\int a^{-1.5}v^3_{\rm drift}(a)da, \quad (9)$$

where the constant A can be calculated from the adopted dust mass-loss rate using equation (4); f is the ratio of atomic-to-molecular hydrogen.

2.2.2. *Rotational Excitation of* H_2O *Molecules*

For an O-rich outflow, this mechanism contributes significantly to the cooling of the envelope. Rotationally excited H_2O molecules can emit photons, which, if they escape from the circumstellar shell, will cool the gas. The structure of an H_2O molecule is complicated, and, following GS, is approximated by a three-level system: two rotational levels in the ground electronic vibrational state at energy $\sim kT$ and one rotational level in $v = 1$. The cooling rate per unit volume between the pure rotational levels is given by

$$C_1 = n_{\rm H_2}(1 + f)hv_{21}n_{\rm H_2O}\langle\sigma^* v_{\rm th}\rangle \times [\exp(-hv_{21}/kT) - \exp(-hv_{21}/kT_x)], \quad (10)$$

where T_x is the rotational excitation temperature; $\langle\sigma^* v_{\rm th}\rangle$ is the collisional rate constant ($= 2 \times 10^{-11}T^{0.5}$ cm^3 s^{-1}); and v_{21} is the transition frequency ($= 2.6 \times 10^{11}T_x^{0.5}$ s^{-1}). The excitation temperature can be calculated from the rate equa-

tion, using an escape probability formalism to describe the radiative transfer in the line.

$$C(\mathrm{H_2O})\frac{h\nu_{21}}{k}\left(\frac{1}{T_x}-\frac{1}{T}\right)=\beta_{21}A_{21}+\frac{1}{2}\epsilon W A_{31}\times\left(\frac{h\nu_{21}}{k}\right)\exp\left(\frac{-h\nu_{31}}{kT_*}\right)\left(\frac{1}{T_*}-\frac{1}{T_x}\right), \quad (11)$$

where ν_{21} and ν_{31} ($=1.13\times10^{14}$ s^{-1}) are the transitional frequencies; $\epsilon=(d\ln v/d\ln r)$ is the velocity gradient; $C(\mathrm{H_2O})$ is the collision rate ($=2\times10^{-11}T^{0.5}n_{\mathrm{H_2}}[1+f]$ s^{-1}); W is the dilution factor for the stellar radiation; β_{21} is the escape probability; and A_{21} and A_{31} ($A_{31}=34$ s^{-1}) are the Einstein A-coefficients. The factor $\frac{1}{2}$ in the front of the last term has been added to correct a typo in the original expression, and similarly for the expression of ν_{21}, a factor of 2 must be multiplied to GS's expression (M. Groenewegen, 1993 private communication). The escape probability can be calculated by

$$\beta_{21}A_{21}=\frac{6.57}{n_{\mathrm{H_2O}}}\frac{v}{r}\left(1+\frac{\epsilon}{2}\right)T_x^3. \quad (12)$$

2.2.3. *Vibrational Excitation of* $\mathrm{H_2}$ *Molecules*

The cooling by $\mathrm{H_2}$ molecules must be treated differently from $\mathrm{H_2O}$ molecules, because they lack a dipole moment and the energy levels are widely spaced. Due to their low Einstein A-values, the lines are optically thin. Moreover, $\mathrm{H_2}$ is in LTE through a larger part of the envelope. The large energy spacing allows us to consider only the ground and the first vibrationally excited level. The molecules are excited by collision with themselves and with H atoms. The heat loss per unit volume is

$$C_2=A_{1,0}h\nu_{10}n_1, \quad (13)$$

where $A_{1,0}$ is the spontaneous emission rate from the first vibrationally excited state, $h\nu_{1,0}$ is the energy of the emitted photon, and n_1 is the number density of vibrationally excited $\mathrm{H_2}$ molecules, which is evaluated to be

$$n_1=n_{\mathrm{H_2}}\left[\frac{(n_{\mathrm{H}}\langle\sigma^*v_{\mathrm{th}}\rangle_{\mathrm{H}}+n_{\mathrm{H_2}}\langle\sigma^*v_{\mathrm{th}}\rangle_{\mathrm{H_2}})\exp(-h\nu_{1,0}/kT)}{\{(n_{\mathrm{H}}\langle\sigma^*v_{\mathrm{th}}\rangle_{\mathrm{H}}+n_{\mathrm{H_2}}\langle\sigma^*v_{\mathrm{th}}\rangle_{\mathrm{H_2}})\times[1+\exp(-h\nu_{1,0}/kT)]+A_{1,0}\}}\right], \quad (14)$$

where $\langle\sigma^*v_{\mathrm{th}}\rangle_{\mathrm{H}}$ and $\langle\sigma^*v_{\mathrm{th}}\rangle_{\mathrm{H_2}}$ are the de-excitation rate constants for collision of vibrationally excited $\mathrm{H_2}$ molecules with H atoms and $\mathrm{H_2}$ molecules, respectively (see GS).

2.2.4. *Rotational Excitation of* CO *Molecules*

Another molecule which is always present in the circumstellar envelope is CO. GS ignored its cooling effect, but we include it here to see how it affects the temperature of O-rich stars. Similar to the calculation for $\mathrm{H_2O}$ rotational cooling, the formulation for CO rotational cooling is given by

$$C_3=n_{\mathrm{H_2}}(1+f)n_{\mathrm{CO}}\langle\sigma^*v_{\mathrm{th}}\rangle\times h\nu\left[\exp\left(-\frac{h\nu_{21}}{kT}\right)-\exp\left(-\frac{h\nu_{21}}{kT_x}\right)\right], \quad (15)$$

where $\nu_{21}=4.89\times10^{10}T_x^{0.5}$ s^{-1}, and T_x is the excitation temperature for CO molecules defined in a similar manner to equation (11), using the three-level atom approximation:

$$C(\mathrm{CO})\frac{h\nu_{21}}{k}\left(\frac{1}{T_x}-\frac{1}{T}\right)=\beta_{21}A_{21}+\frac{1}{2}\epsilon W A_{31}\left(\frac{h\nu_{21}}{k}\right)\exp\left(\frac{-h\nu_{31}}{kT_*}\right)\left(\frac{1}{T_*}-\frac{1}{T_x}\right), \quad (16)$$

where $C(\mathrm{CO})=10^{-11}T^{0.5}n_{\mathrm{H_2}}(1+f)$ s^{-1}, $\nu_{31}=6.43\times10^{13}$ s^{-1}, $A_{31}=34$ s^{-1}, and the escape probability is defined as

$$\beta_{21}A_{21}=\frac{6.60}{n_{\mathrm{CO}}}\frac{v}{r}\left(1+\frac{\epsilon}{2}\right)T_x^{2.5}. \quad (17)$$

2.2.5. *Vibrational Excitation of* $\mathrm{H_2O}$ *Molecules*

In view of the high critical density, collisional excitation followed by radiative decay of vibrational levels of $\mathrm{H_2O}$ is unimportant for the cooling of the gas and can safely be ignored. GS incorrectly identify the reaction $\mathrm{OH}+\mathrm{H_2}\rightarrow\mathrm{H_2O}+\mathrm{H}+0.67$ eV as a cooling term for the gas. This reaction is actually exothermic in the forward direction. It leaves $\mathrm{H_2O}$ in a vibrational excited state (Schatz & Elgersma 1980). While this vibrational fraction ($\sim$56%) of the excess chemical energy is lost through radiative cooling, about 35% of the total energy is converted to translational energy which heats the gas. The remainder goes into rotational excitation. After taking the activation barrier ($\sim$0.27 eV) into account, the net heating of the gas is about 0.1 eV per reaction. In comparision with other heating sources, this is small and is neglected in the calculations.

The reverse reaction is endothermic and thus leads to cooling of the gas. However, its rate is dependent on the vibrational excitation of $\mathrm{H_2O}$. Since the foward reaction leads to vibrational excitation, the reverse reaction requires vibrationally excited $\mathrm{H_2O}$ from detailed balance. This is born out by detailed calculations, which show that the reverse rate is reduced by a factor of 100 for $\mathrm{H_2O}$ in $v=0$ level (Herbst & Knudson 1981). As a result, in the envelope where the density is below the critical density for $\mathrm{H_2O}$, the reverse reaction is frozen out and consequently plays no role in the energy balance. Finally, we note that near the photosphere where $\mathrm{H_2O}$ is in LTE, the foward and backward reactions do not lead to significant net heating or cooling of the envelope.

2.2.6. *The Energy Balance*

In order to calculate the temperature as a function of radius, all the described processes must be taken into account. The total cooling rate is

$$C_{\mathrm{tot}}=C_1+C_2+C_3. \quad (18)$$

Hence, the temperature structure of the envelope, i.e., the gas kinetic temperature, is governed by

$$\frac{1}{T}\frac{dT}{dr}=\frac{-4}{3r}\left(1+\frac{\epsilon}{2}\right)+\frac{2(H-C_{\mathrm{tot}})}{3vn_{\mathrm{H_2}}kT(1+f)}, \quad (19)$$

where the first term on the right-hand side represents the cooling by adiabatic expansion.

The inner boundary condition for solving the above differential equation is the specification of the grain condensation radius, r_i, where the dust temperature falls below 1000 K for silicates. For a given dust mass-loss rate, this inner radius follows from the solution of the radiative transfer problem. Dust grains are assumed to form at the local drift velocity. We

also need to input the stellar mass, the effective temperature, the dust mass-loss rate, and the dust-to-gas mass ratio. Once we specify all these values, the code proceeds to calculate the radiation pressure efficiencies, averaged over the stellar luminosity for each grain size, in order to calculate Γ from equation (7), which is then used to solve for the velocity at point r (eq. [1]). Hence, the density structure can be determined, along with the heating and cooling rates, which enable us to solve for the gas kinetic temperature of the envelope.

From the earlier discussion, we know that the heating and cooling mechanisms are dependent on the flow of the gas. We now look at how the velocity is affected by changes in the stellar parameters. Increasing the stellar effective temperature, or the stellar radius results in an increase in the stellar luminosity, and since $v \propto L$, the velocity increases as well. Since this also means an increase in the drift velocity, the heating rate increases by a large factor ($H \propto v_{\rm drift}^3$). The increased velocity also affects the cooling, since photons escape more easily, i.e., T_x depends on v (see eq.[12]). However, the cooling rate does not increase by the same factor, which results in a higher gas kinetic temperature throughout the envelope.

The assumed stellar mass affects the terminal velocity, since the gas will require more energy to overcome the stronger gravitational force of the star (eq. [1]). By increasing the stellar mass by a factor of 2, the terminal velocity decreases by a small factor, roughly as $M^{0.5}$. Since this has a very small effect on the velocity flow, the temperature is hardly altered by an increase in the stellar mass. The escape velocity is also influenced by the inner radius of the shell. Thus, increasing the radius where dust condenses out will decrease the terminal velocity of the gas ($v \propto v_{\rm esc} \propto r_i^{-1/2}$). Both heating and cooling rates are only slightly affected, so the overall result is a small increase in the temperature, for a factor of 2 increase in the dust condensation radius. Changing the ratio of the atomic-to-molecular hydrogen does not affect the velocity or the heating rate but changes the cooling rates slightly. The overall effect is a very small change on the temperature structure. The results show that gas kinetic temperature is insensitive to small changes (a factor of 2) in the input parameters. Any changes in the heating rates are compensated by similar changes in the cooling rates, which retain the gas temperature to within the same range of values.

The main parameter that influences the structure of circumstellar shells is the mass-loss rate. The observed mass-loss rates for asymptotic giant branch (AGB) stars range from 10^{-7} to $10^{-4}\ M_\odot\ {\rm yr}^{-1}$. A higher mass-loss rate yields a higher terminal velocity of the flow, since there is more dust to intercept the radiation and hence to accelerate the gas by the transfer of its momentum. However, there comes a point where increasing the mass-loss rate has little effect on the terminal velocity. This occurs when the drift velocity is low compared to the gas velocity. The influence of mass-loss rate on the temperature structure of the envelope is quite complex. The increase in the mass-loss rate has a direct consequence on the drift velocity (eq. [6]) and thus on the viscous heating rate, which scales as $H \propto \dot{M}^{0.5} v^{1.5}$. The high mass-loss rate influences "cooling" rates in two ways. First, the increase in the dust emission leads to a higher infrared pumping rate. Coupled with the increased density in the envelope, collisional de-excitation of vibrationally pumped H_2O and CO molecules is important over a larger part of the envelope. Second, the increase in the density leads to a higher H_2O cooling rate per unit volume in the outer part of the envelope. It should be noted that since the rotational transitions are highly optically thick, the rotational levels are close to LTE, and hence the cooling rate per H_2O molecule is largely independent of the density (i.e., mass-loss rate). Now, for low mass-loss rates ($\dot{M}_d \leq 10^{-7}\ M_\odot\ {\rm yr}^{-1}$). the second effect dominates, and an increase in the mass-loss rate results in a slightly cooler outer envelope. For high mass-loss rates ($\dot{M}_d \geq 10^{-7}\ M_\odot\ {\rm yr}^{-1}$), the first effect dominates, and the enhanced heating over the inner envelope results in an increase in the temperature over the entire outflow.

3. MODELING O-RICH STARS

The stars chosen are taken from a sample for which dust mass-loss rates have been determined from their infrared continuum observations (Justtanont & Tielens 1992). They have been selected on the grounds that they have dust mass-loss rates which cover a wide range, from 7.2×10^{-9} to 1.2×10^{-6} $M_\odot\ {\rm yr}^{-1}$ and have been well studied in their CO emission. Results will be discussed source by source. The input parameters required for each star are listed in Table 1, most of which are taken from the infrared modeling (Justtanont & Tielens 1992), namely, stellar effective temperatures, stellar radii, and dust condensation radii. Cosmic carbon and oxygen abundances have been assumed throughout (Anders & Grevess 1989). The gas mass-loss rate is calculated by specifying the dust mass-loss rate and the dust-to-gas mass ratio, δ. The parameter δ is adjusted so that the value of the observed terminal velocity is obtained. The code then calculates the velocity, density, and gas kinetic temperature as a function of radius. The final temperature structure will be used in the calculations of the CO line profiles in the next section.

3.1. *GX Monocerotis*

This star has a 10 μm silicate feature strongly in emission, which implies that its envelope is optically thin. Its spectrum peaks around 1.2 μm; hence, the effective temperature is about 2500 K. Its wind terminal velocity, measured from the observed CO line is 19 km s^{-1}. The stellar radius and the condensation radius are taken from infrared modeling.

We obtain the terminal velocity of 19 km s^{-1} for GX Mon for $\dot{M}_d = 3.4 \times 10^{-8}\ M_\odot\ {\rm yr}^{-1}$ and $\delta = 4.7 \times 10^{-3}$, which translates to a gas mass-loss rate of $7.2 \times 10^{-6}\ M_\odot\ {\rm yr}^{-1}$. The velocity acceleration zone extends out to 10^{16} cm. The dust

TABLE 1

INPUT PARAMETERS FOR THREE O-RICH STARS

Star	T_* (K)	M_* ($M_\odot$)	R_* (cm)	R_i (cm)	$\dot{M}_d$ ($M_\odot$ yr^{-1})	$\dot{M}_d/\dot{M}$ (δ)	$\dot{M}$ ($M_\odot$ yr^{-1})
GX Mon	2500	1.0	4.0E+13	2.5E+14	3.4E−08	4.7E−03	7.2E−06
IRC +10011	2000	1.0	4.5E+13	1.8E+14	5.9E−08	5.9E−03	1.0E−05
OH 26.5+0.6	2200	1.5	5.0E+13	3.1E+14	2.4E−07	2.4E−03	1.0E−04

NOTES.—Input parameters for three chosen O-rich stars for calculation of the gas kinetic temperature

drift velocity for a star with such a low mass-loss rate is large, compared to the gas velocity, since dust grains do not collide with the gas often enough to transfer much of their momentum to the gas; hence, they drift rapidly (7.5 km s^{-1}) outwards (see Fig. 1).

At the innermost radius where dust condenses, H_2O and CO rotational excitations contribute to the heating, rather than cooling, of the gas. This is due to the fact that in this region, the excitation temperatures of these molecules are higher that the gas kinetic temperature. As a result of the large drift velocity throughout the envelope, heating by gas-grain collision dominates over other heating processes.

Adiabatic expansion is the dominant cooling mechanism at large distances from the star, while H_2O cooling dominates in the region between $4 \times (10^{14}$–$10^{16})$ cm. It can be clearly seen from Figure 1 that H_2O rotational cooling is much more efficient throughout the envelope than CO rotational cooling. Cooling rates decrease with increasing radius due to decreasing number densities of the molecules. Cooling by H_2 vibrational excitation is only significant in the inner part of the envelope and drops off sharply once the density drops below the critical density for LTE condition.

The resulting temperature structure clearly does not follow a simple power law, as has been assumed for gas kinetic temperature in circumstellar envelopes by various authors (see e.g., Schonberg 1988; Wattenbach et al. 1988). The temperature drops off rapidly ($T \propto r^{-1.2}$) in the inner part ($r < 2 \times 10^{15}$), which reflects the efficient cooling by molecules. In the outer parts, the temperature law can be approximated by $T \propto r^{-0.56}$.

For the mass-loss rate of GX Mon, the CO photodissociation radius is approximately 2.8×10^{17} cm (see § 4.3). In principle, this effect reduces the cooling rate for GX Mon beyond the photodissociation radius. However, at this radius, CO cooling is negligible compared to either H_2O or the adiabatic cooling; hence, this does not affect the final gas kinetic temperature. At this radius the temperature is about 12 K, comparable to the ambient interstellar medium.

3.2. *IRC+10011*

Here, we can make a comparison between our model (Fig. 2) and that calculated by GS. There are major differences which must be born in mind when comparing the two results. We include a grain size distribution, using silicate optical constants which fit the observed infrared spectrum, excluded H_2O vibrational cooling, and included CO rotational cooling. From the constraint of the observed terminal velocity, the gas mass-loss rate is determined to be $1 \times 10^{-5}\ M_\odot\ yr^{-1}$, which is smaller than the value of $3 \times 10^{-5}\ M_\odot\ yr^{-1}$ adopted by GS. The stellar radius, derived from the infrared continuum model, is 4.7×10^{13} cm, as opposed to 6×10^{13} cm in the GS model.

Whereas GS arbitrarily adopted an average radiation pressure efficiency of 0.5, our calculated value turns out to be much smaller, 0.03. GS adopted a rather arbitrary density (e.g., velocity) law. In our model, the rise in velocity is much steeper than in theirs. This has a profound effect on all other calculated values, since the flow determines the density structure in the envelope. As expected from the smaller radiation pressure efficiency and difference in grain sizes, we obtain a lower drift velocity of 4.5 km s^{-1} (for the largest grain size), as opposed to

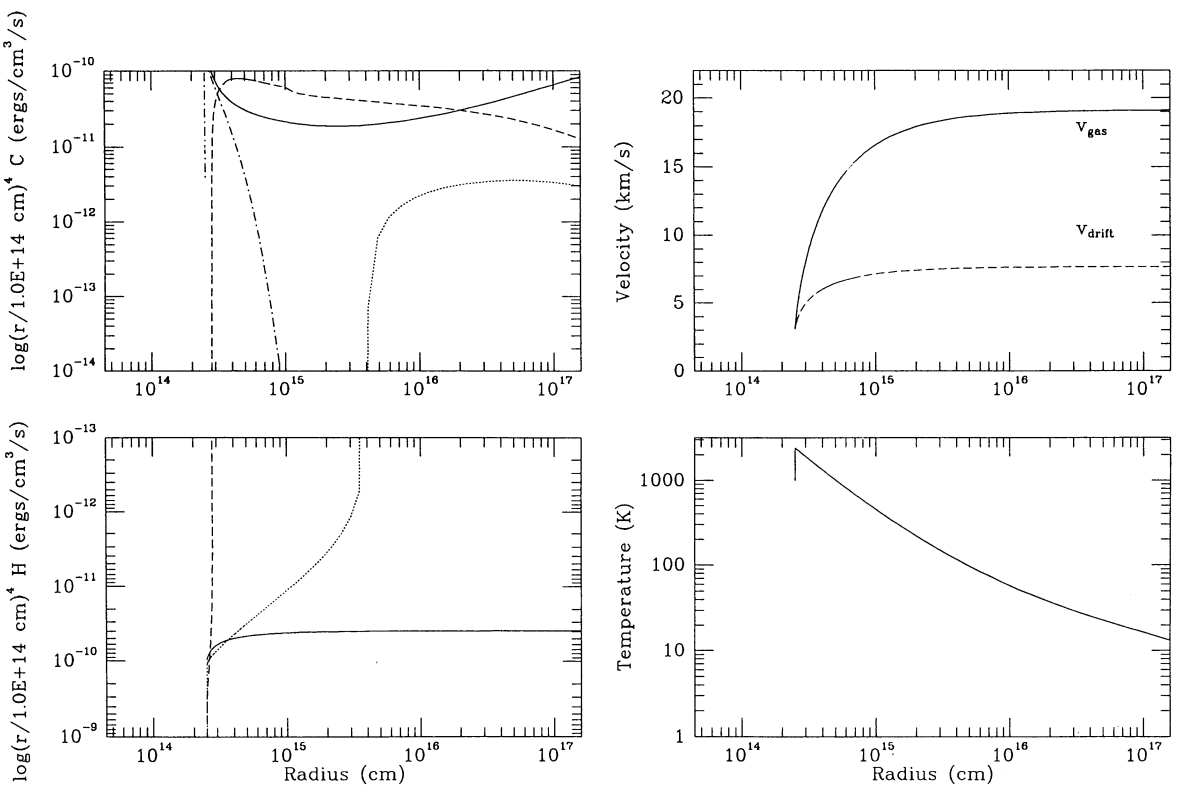

FIG. 1.—The resulting gas kinetic temperature from the calculation of heating and cooling in the circumstellar envelope of GX Mon with $\dot{M}_d = 3.4 \times 10^{-8}\ M_\odot\ yr^{-1}$ and $\delta = 4.7 \times 10^{-3}$. In the cooling panel, the solid line is cooling by adiabatic expansion; the dot-dash line is the cooling by vibrationally excited H_2; the dashed line and dotted line are cooling rotationally excited H_2O and CO, respectively. In the heating panel, the solid line is the heating by gas-grain collision; and the dashed line and dotted line are by H_2O and CO, respectively.

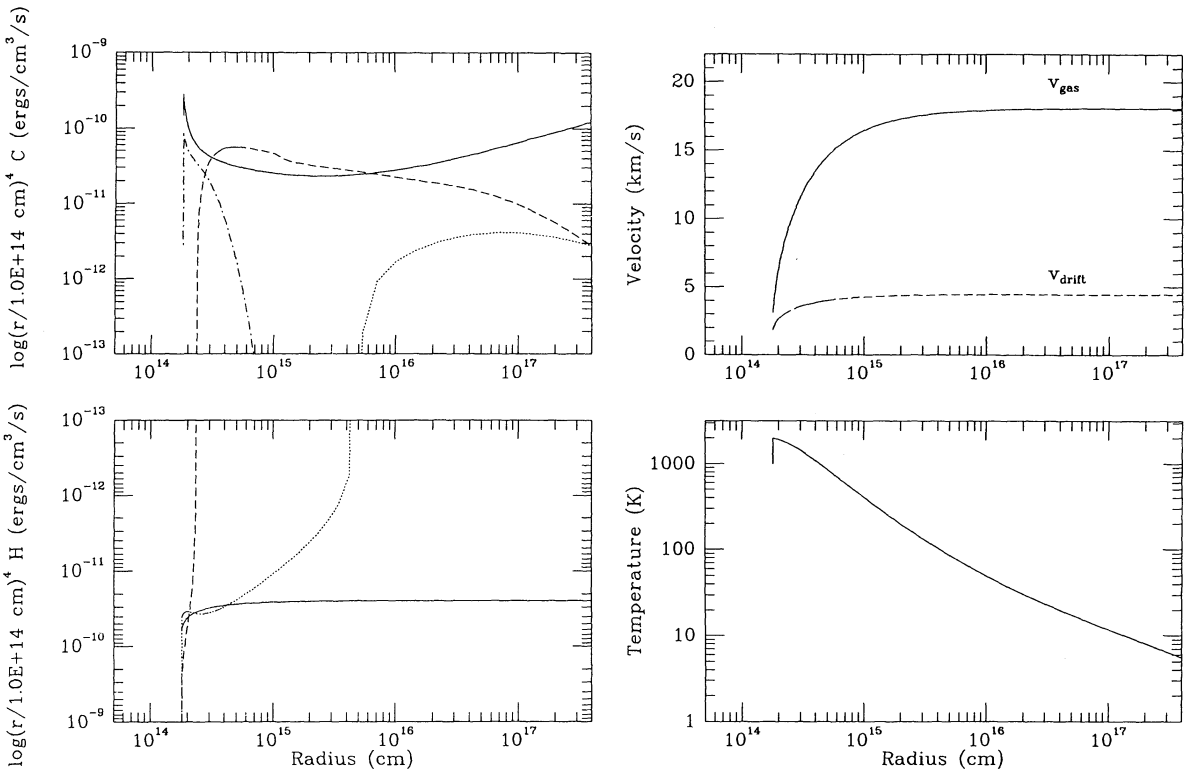

FIG. 2.—The resulting gas kinetic temperature for IRC +10011 with $\dot{M}_d = 5.9 \times 10^{-8}\ M_\odot\ \mathrm{yr}^{-1}$ and $\delta = 5.9 \times 10^{-3}$

9 km s^{-1} by GS. Because of this, the heating rate is less than that obtained by GS.

The heating radii for both H_2O and CO rotations shift outward compared to GX Mon, since the infrared pumping is more important. However, the cooling by vibrationally excited H_2 is comparable for the two stars. Although IRC +10011 has higher H_2 density, its effective temperature is lower than GX Mon. The final temperature is therefore different between the two stars. In the GS model, the combination of the arbitrarily adopted slow rise in the gas velocity and the resulting density structure gives a plateau of the temperature near the inner radius. In our model, the plateau is not present. In the inner part ($r < 2 \times 10^{15}$ cm), the temperature decreases more rapidly then varies approximately as r^{-1}, and the slope becomes less steep beyond 10^{16} cm. It is evident that the slopes of IRC +10011 and GX Mon (see Figs. 1 and 2) are different for both inner and outer parts of the envelopes. The difference in mass-loss rates and velocity structures results in different density distributions and hence heating and cooling rates.

3.3. *OH 26.5+0.6*

In modeling the infrared energy distribution of this source, we have to modify the optical constants in order to get a ratio of 20:10 μm of 0.8 (Bedijn 1987; Justtanont & Tielens 1992). We used these values to calculate the radiation pressure efficiencies as input values for our gas outflow model. The high dust mass-loss rate and the constraint of the terminal velocity implies that the gas mass-loss rate is $5 \times 10^{-4}\ M_\odot\ \mathrm{yr}^{-1}$ which is very high. From the high dust and gas mass-loss rate, this source seems to be in a superwind phase.

In modeling the gas kinetic temperature, we arbitrarily assumed that the mass-loss rate is $10^{-4}\ M_\odot\ \mathrm{yr}^{-1}$, which is a more typical value for OH/IR stars with a thick envelope. Due to the high gas density in the envelope, the transfer of momentum from dust grains to gas is very efficient, resulting in very small drift velocity of the grains (Fig. 3). Although the drift velocity is low (2 km s^{-1}), the density is very high, hence the viscous heating rate of this source is higher than for the previous sources discussed. The optical constants used for this source give higher radiation pressure efficiencies. Also, due to the high density, the heating by H_2O and CO rotational excitation is maintained out to a large distance. Likewise, the cooling rate per unit volume due to adiabatic expansion is also higher due to higher velocity. From Figure 3, it is seen that H_2 cooling plays an important role, partly due to the high density and partly due to the higher stellar effective temperature as compared to IRC +10011. This high density results in lower temperature in the outer part of the envelope since there are more H_2O molecules present. Because of the very high mass-loss rate, CO self shielding against photodissociation is very effective, and so the photodissociation radius for this source is very large, extending to 2×10^{18} cm, where the temperature is just below 3 K. In reality, the temperature can, of course, never fall below the 2.73 K background.

An important source of heating in the outer part of the envelope which we have not considered is photoelectric heating by UV photons in the incident interstellar radiation field. This mechanism could be very important for very optically thick envelopes and will raise the gas temperature. However, photoelectric heating is dominated by very small grains (radii less than 100 Å; see Bakes & Tielens 1994). Observations show that such small silicate grains are probably not present in the interstellar medium. While this does not necessarily preclude their presence in circumstellar shells, they are probably not abundant in oxygen-rich outflows. In the CO modeling of this source in § 4.5, we argue that the outer part of

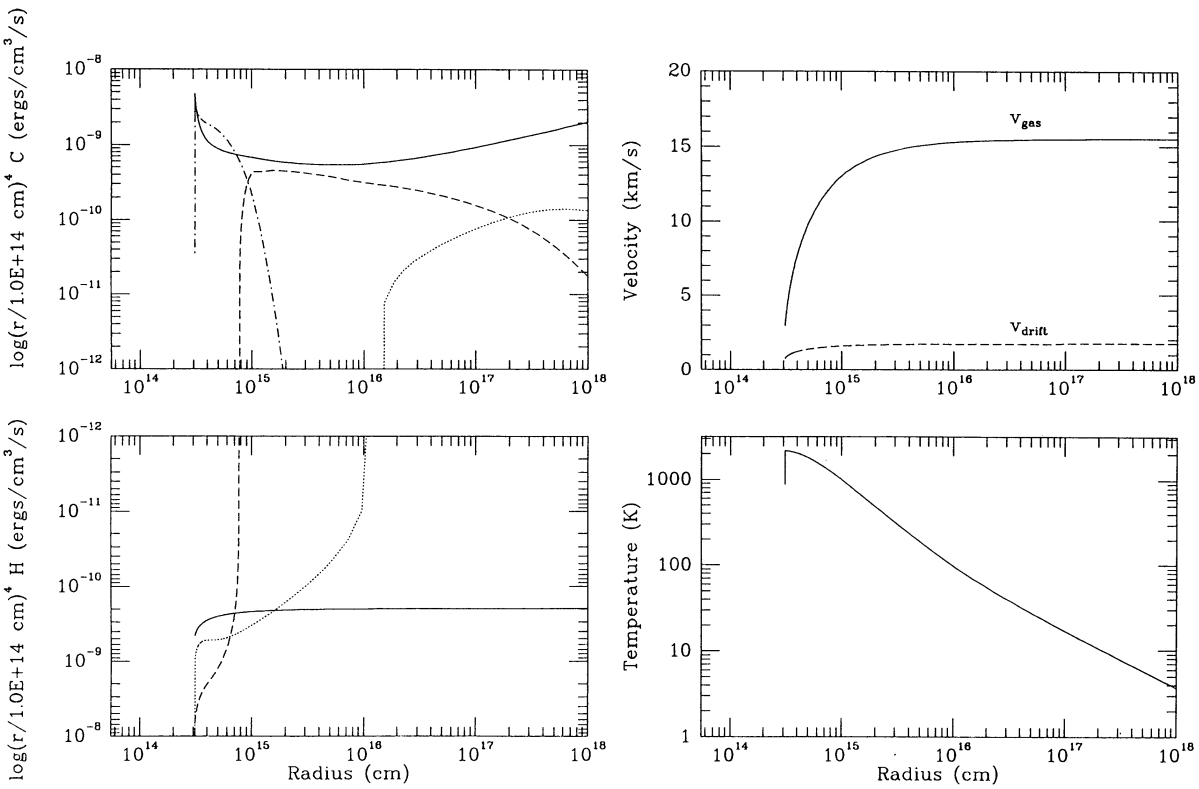

FIG. 3.—The resulting gas kinetic temperature for OH 26.5+0.6 with $\dot{M}_d = 2.4 \times 10^{-7}\ M_\odot\ \mathrm{yr}^{-1}$ and $\delta = 2.4 \times 10^{-3}$

the circumstellar shell of this source is more tenuous. Hence, this heating mechanism plays a very small role and is therefore ignored. We note, however, that for carbon-rich outflows photoelectric heating might be more relevant.

4. CO EMISSION FROM CIRCUMSTELLAR ENVELOPES

Morris (1975) calculated the dependence of CO $J = 1$–0 line profiles on various physical parameters. His approach was simple and approximate, but yielded reasonable results. Bujarrabal & Nguyen-Q-Rieu (1981) presented a more detailed radiative method for molecular lines, which applied the Sobolev approximation, i.e., assuming a negligible turbulent velocity. However, for a typical outflow velocity of a late-type star (10–20 km s^{-1}), this is no longer true, since the turbulent velocity is of order 1 km s^{-1}. The use of the Sobolev approximation must be avoided if the correct line profile is to be obtained. This is discussed in detail by Hamann (1981) and Schonberg (1985). The latter author showed that the validity of the Sobolev approximation depends not only on the ratio of the macroscopic and stochastic velocities, but also on the opacity structure. The method of the comoving frame for a two-level atom was developed by Mihalas, Kunaz, & Hummer (1975, hereafter MKH), based upon an elimination scheme, which greatly facilitated the computation of the line transfer in spherically expanding atmospheres. However, this fails for a multilevel system, since the occupation numbers become nonlinear.

4.1. *The Radiative Transfer Code*

The radiative transfer code used to model emission lines in the millimeter region is based on the work by Hempe & Schonberg (1986). It was originally designed to solve for the occupation numbers for two-level atoms in the comoving frame using the approximate Newton-Raphson (ANR) technique. This allows for a faster convergence compared to the conventional Λ iteration, especially in the optically thick envelopes. The method has been adapted by Schonberg & Hempe (1986) to cope with multilevel species. Here we apply it to account for the first 11 rotational transitions in the ground and first excited vibrational states of CO.

The rate equation can be written as

$$F_l = n_i \sum_{j \neq i} (A_{ij} + C_{ij} + B_{ij} \Lambda_{ij} S_{ij}) - \sum_{j \neq i} n_j (A_{ji} + C_{ji} + B_{ji} \Lambda_{ij} S_{ij}) = 0\ , \quad (20)$$

where $A_{i,j}$, B_{ij}, and B_{ji} are Einstein's A- and B-coefficients, C_{ij} is the collisional rates, Λ_{ij} is the Λ operator, and S_{ij} is the source function. With starting occupation numbers, the code calculates the source function and opacities and then solves the transfer equation and calculates the scattering integral and its derivative for each line, using the ANR operator. These are stored as matrix elements which are then inverted in order to calculate the occupation numbers for the next iteration. This is done until the difference between each successive iteration is smaller than some specified number. The results are then said to be convergent. The CO collisional cross sections with H_2 are taken from McKee et al. (1982) and Flower & Launay (1985). Data on the $v = 1$–0 transition are from Chackerian (1976) and Stricker (1978), with other molecular data from Huber & Herzberg (1979). A total of 12 rotational levels are treated in both $v = 0$ and $v = 1$ vibrational levels with all allowed rovibrational transitions.

After solving the radiative transfer for molecular lines in circumstellar shells, line profiles for each transition can then be calculated by formal integration (Schonberg 1988). The line shape reflects the optical depth effects of each line, e.g., for optically thin lines, the profiles are double peaked, while optically thick lines are crudely parabolic (e.g., Morris 1975). The flux, however, is dependent on the assumed distance and the telescope beam widths.

To emphasize the importance of correctly handling the radiative transfer, and of avoiding the use of Sobolev approximation, we show in Figure 4 three models for the CO $J = 1$–0 line in the star IRC +10011, using stochastic velocities of 0.1, 0.5, and 1.0 km s^{-1}. All other parameters in the models remained fixed. As can be seen, both the peak antenna temperature and the line shape are affected significantly. At small stochastic velocities (0.1 km s^{-1} or less) the Sobolev approximation is valid (Schonberg 1985), and our model yields a parabolic line profile. With larger stochastic velocity, the Sobolev approximation ceases to be valid, and we obtain a flatter topped, lower intensity line because the column density is decreased. For a more detailed discussion of the validity of the Sobolev approximation in molecular rotational line profiles, the interested reader should refer to Schonberg (1985).

4.2. CO *Emission from the Three* O-*rich Stars*

Here, we combine the results from § 3 in order to get a comprehensive model of dust and gas mass-loss rates for the same stars. The gas kinetic temperature, along with previously used parameters, are used as inputs for the CO code to get a more consistent picture of processes going on in the circumstellar envelopes. Such a self-consistent model has been calculated only for C-rich stars (Sahai 1990). Although Kastner (1992) modeled O-rich stars, H_2O cooling was not included in his study. This results in higher gas kinetic temperatures in our models. However, the difference is more pronounced in the case of low mass-loss rate.

The inputs are listed in Table 2 for the three stars, GX Mon, IRC +10011 and OH 26.5+0.6. The dust mass-loss rates are determined from the modeling of the observed infrared continuum. The dust temperature distribution has been approximated by the power law

$$T_d(r) \propto \left(\frac{r}{R_*}\right)^{-\eta}, \tag{21}$$

where η is obtained from the detailed models of the infrared energy distribution of each star (Justtanont & Tielens 1992). Although the dust temperature is not strictly a simple power law, due to back heating of dust in the inner part of the circumstellar shell, we can approximate η to a single number without seriously affecting the actual values. The dust-to-gas mass ratio, and hence the gas mass-loss rate, follow from solving the momentum equation, which results in the observed terminal velocity. The gas temperature distribution is then derived from the energy equation (see § 3).

For O-rich stars, all the elemental carbon is locked up in CO in the photosphere. Hence, the CO abundance is given by the elemental carbon abundance. In the outer part of the envelope, the CO abundance is mainly governed by the penetration of UV radiation from the interstellar medium. Essentially, this process leads to an outer radius beyond which CO is photodissociated. Mamon, Glassgold, & Huggins (1988), using the new photodissociation rate from Letzelter et al. (1987), obtained the following expression for the CO abundance

$$x = x_0 \exp\left[-\ln 2\left(\frac{r}{r_{1/2}}\right)^{\alpha}\right], \tag{22}$$

where x and x_0 are the CO abundance at radius r and the initial abundance, respectively, $r_{1/2}$ is the radius where the abundance drops to half the initial value, and α is a parameter determining the run of the density. Mamon et al. (1988) give values of $r_{1/2}$ and α for a large range of mass-loss rates.

TABLE 2

PARAMETERS FOR THREE O-RICH STARS

Source	$\dot{M}$ ($M_\odot$ yr^{-1})	D (pc)	η	$T_A(J = 1$–$0)$	$T_A(J = 2$–$1)$
GX Mon[a]	7.2E−6	740	0.54	0.51	1.42
IRC +10011[b,c]	1.0E−5	680	0.58	0.21	1.08
OH 26.5+0.6[d]	1.0E−4	1000	0.58	0.24	1.72

NOTES.—Parameters for the three O-rich stars under investigation, where η is the index for dust temperature as a function of distance. The predicted temperatures are calculated for parameters appropriate for data from the following (see footnotes).

[a] SEST (this paper).

[b] Knapp & Morris 1985.

[c] Knapp et al. 1982.

[d] Heske et al. 1990.

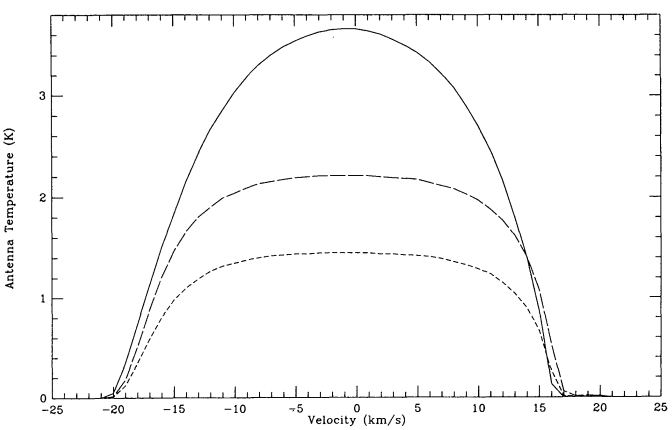

FIG. 4.—Line profiles calculated for the CO $J = 1$–0 line in IRC +10011 using models with all parameters kept identical except for the stochastic (turbulent) velocity which was set to 0.1 km s^{-1} (*solid line*), 0.5 km s^{-1} (*long-dashed line*) or 1 km s^{-1} (*short-dashed line*). Note that both the line shape and intensity are affected strongly.

4.3. *GX Monocerotis*

For this source, we observed both the $J = 1$–0 and 2–1 lines with the Swedish ESO Submillimeter Telescope (SEST), which has a diameter of 15 m and a beam size of 44″ and 22″, respectively. Both lines have been corrected for beam efficiency and atmospheric extinction (Fig. 5). From the observed profiles, the velocity for the outer envelope is 19 km s^{-1}, which is slightly higher than the OH maser velocity of 17.5 km s^{-1} (te Lintel Hekkert et al. 1989). The observed $J = 2$–1 line is optically thick, since it takes on a parabolic shape, while the $J = 1$–0 line is flat. With an expected CO photodissociation radius of 2.8×10^{17} cm (26″ at 740 pc), this source is unresolved for the 1–0 transition. The calculated ratio of the antenna temperatures of the two lines is 2.8, while the observed is 1.6. The

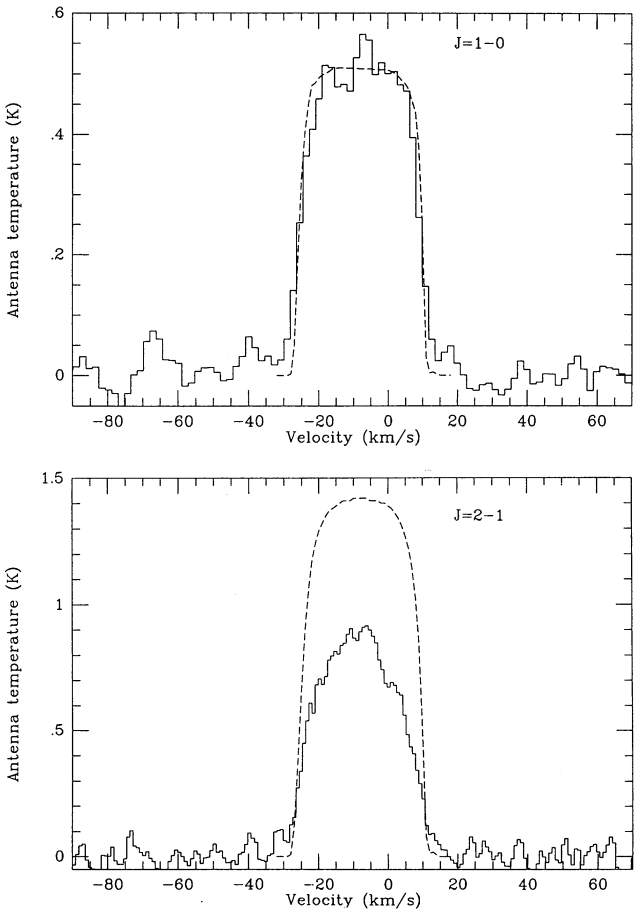

FIG. 5.—The line profiles of GX Mon for $J = 1$–0 and $J = 2$–1 transitions, as observed from SEST (*solid line*). The fitted profiles (*dashed line*) are calculated using temperature structure previously computed.

best-fit profile for $J = 1$–0 line is obtained with a mass-loss rate of $7.2 \times 10^{-6}\ M_\odot\ \mathrm{yr}^{-1}$ and a distance of 740 pc (Fig. 5; Table 2). However, this model overestimates the antenna temperature of the $J = 2$–1 line. Our result for this line exceeds the observed temperature by a factor of 1.5.

The dust mass-loss rate derived from our CO modeling ($3.4 \times 10^{-8}\ M_\odot\ \mathrm{yr}^{-1}$) is somewhat larger than from the mid-infrared modeling ($7.2 \times 10^{-9}\ M_\odot\ \mathrm{yr}^{-1}$). Since infrared emission originates close to the star, while the CO originates in the outer part of the shell, this may imply that mass loss has decreased over the last 5000 yr. The discrepancy between the observed and calculated 2–1 antenna temperature may reflect this decrease in the mass-loss rate with time or may be due to the calibration of the line. The latter can be uncertain by a factor of 30% (R. Sahai, 1993, private communication).

There are also other data available for this source. For example, Margulis et al. (1990), who used the 14 m telescope of the Five College Radio Astronomy Observatory (FCRAO) with a beam size of 45″ to observe the $J = 1$–0 line, report a main beam temperature of about 0.4 K. From our calculation, using the input parameters which fit the SEST $J = 1$–0 data, we arrive at an antenna temperature of 0.44 K for the FCRAO telescope, which is close to the observed value. The observed profile is flat, which is in good agreement with the calculated profile.

4.4. *IRC +10011*

The data on IRC +10011 were obtained from Knapp et al. (1982) for the $J = 2$–1 transition, and Knapp & Morris (1985) for the $J = 1$–0 transition. The $J = 2$–1 line profile is more rounded than the $J = 1$–0 line, indicative of a higher optical depth for the former. The calculated antenna temperature of the $J = 1$–0 line agrees quite well with the observations. In order to match profiles and the peak antenna temperatures, the distance is taken to be 850 pc rather than the usually cited 500 pc (Hyland et al. 1972), which is still within the estimated uncertainties. The gas mass-loss rate derived from previous CO analysis is $1.0 \times 10^{-5}\ M_\odot\ \mathrm{yr}^{-1}$ (Knapp & Morris 1985), which is the same as our calculated value from the radiation pressure driven wind. In order to drive the outflow at 18 km s^{-1}, the dust mass-loss rate is taken to be $5.9 \times 10^{-8}\ M_\odot\ \mathrm{yr}^{-1}$, compared to $1.4 \times 10^{-7}\ M_\odot\ \mathrm{yr}^{-1}$, estimated from the mid-infrared modeling (Justtanont & Tielens 1992). This may indicate the star is losing mass at a higher rate than in the past, since the infrared emission originates from a region much closer to the star than for CO.

Knapp et al. (1982) observed this source with the Caltech 10 m telescope using a beam size of 30″. They obtained a temperature of 2.8 K for the $J = 2$–1 transition. Knapp & Morris (1985) obtained a value of 0.18 K for the $J = 1$–0 transition using the Bell 7 m telescope and a beam size of 100″. Using the appropriate parameters for these telescopes, the antenna temperature calculated from our model for the $J = 2$–1 is 1.08 K, and for the $J = 1$–0 line it is 0.21 K (see Table 2). Sopka et al. (1989) observed the $J = 1$–0 transition with the Onsala 20 m telescope with a beam size of 33″ and obtain a temperature of 0.92 K, while Margulis et al. (1990) used the 14 m telescope at FCRAO with a beam size of 45″ and obtained a temperature of 0.6 K. Our model yields antenna temperatures of 1.44 K and 0.73 K, respectively. Our profiles for both cases have flat tops, which match the observed line profiles. We do not compare our calculated profiles with the published observations since the observed profiles are too noisy. However, the general line shapes and peak antenna temperatures agree well with published values.

4.5. *OH 26.5+0.6*

Extensive model runs show that we cannot reproduce the observed large 2–1/1–0 ratio (>10; see Heske et al. 1990) for any constant mass-loss rate. The low 1–0 temperature of extreme OH/IR stars is a very general problem which may reflect temporal evolution in the mass-loss rate. From the infrared modeling of this star, the calculated dust mass-loss rate is extremely high, $1.2 \times 10^{-6}\ M_\odot\ \mathrm{yr}^{-1}$ (Justtanont & Tielens 1992). This corresponds to the gas mass-loss rate of about $5 \times 10^{-4}\ M_\odot\ \mathrm{yr}^{-1}$, assuming a constant mass-loss rate being driven by radiation pressure. Such a high mass-loss rate suggests that the star may be in a superwind phase. This phase would only last a small fraction of the total lifetime of the AGB phase. Thus, the assumption of the steady mass-loss rate may break down here. There may have been a period in the past when the mass-loss rate was much lower. Indeed, the CO 1–0 emission will originate from near the CO photodissociation radius. With the observed outflow velocity, the timescale to reach this radius is 8×10^4 yr. If the mass-loss rate is assumed to be constant throughout this timescale, the total mass in the envelope will reach 40 $M_\odot$. This is in conflict with stellar evolution theory, which suggests ignition of C-burning in the

central C-O white dwarf for stars more massive than $\sim 8\ M_\odot$ (Iben & Renzini 1983).

In order to model this source correctly, we should take into account the variable mass-loss rates over the past 10^4–10^5 yr. As a first approximation, we take a discontinuity in mass-loss rate, i.e., close to the star, the mass-loss rate is $10^{-4}\ M_\odot\ \mathrm{yr}^{-1}$, and farther out in the envelope, the mass-loss rate is $10^{-6}\ M_\odot\ \mathrm{yr}^{-1}$, which is still a reasonable value for a star on the AGB. We also assume that the gas kinetic temperature has a similar discontinuity. We obtained antenna temperature of 1.72 K for the $J = 2$–1 transition, which is in a good agreement with the observed value from Heske et al. (1990). We estimate the antenna temperature for the $J = 1$–0 transition to be 0.24 K (Table 2). This gives the ratio between the two lines of 7.2. The antenna temperature of the high rotational transitions are thought to be representative of the present high mass-loss nature of the star. In the outer envelope, the density may have been less, assuming that the superwind phase only occurred in the past 200 yr (i.e., the outer radius of the superwind is currently 7.9×10^{15} cm). The density in the outer envelope then represents the density prior to the onset of this superwind phase. With a mass-loss rate of $10^{-6}\ M_\odot\ \mathrm{yr}^{-1}$ in the outer part, the CO photodissociation radius is 10^{17} cm.

4.6. *Predictions of Higher Transition Lines*

Table 3 shows the predicted antenna temperatures for transitions up to $J = 6$–5 line. We assume that the source is observed with a 15 m telescope, using a beam size which is diffraction limited for each transition, i.e., $\theta = 1.22\lambda/d$, where d is the telescope diameter. For GX Mon, it can be seen in Figure 6 that all transitions are optically thick, with the $J = 1$–0 line having a flat-top profile. For high transitions, line shapes become more parabolic. There is a slight asymmetry in the line wing for lower transitions. We see more flux in the front part of the envelope, which is moving toward us, than in the back of the envelope. Similarly, for IRC +10011, the antenna temperature rises as a function of the J value. The profiles start off relatively flat for the $J = 1$–0 transition and become progressively more rounded. The profile at each transition is more rounded than the corresponding one from GX Mon, reflecting the higher mass-loss rate in IRC +10011. As for GX Mon, the line profile is noticeably asymmetric in low transitions, where the blue wing is more extended than the red wing in velocity space.

For OH 26.5+0.6, the temperature keeps increasing for higher J lines, probing closer to the region where the mass-loss rate is higher than in the outer part. The profiles are distinctly parabolic for high transitions.

The observations of high transitions of CO lines are desirable if the nature of mass loss is to be probed at different distances from the central star. This, in turn, will indicate the

TABLE 3

PREDICTED PEAK ANTENNA TEMPERATURES

		T_A (K)		
TRANSITION	BEAMWIDTH	GX Mon	IRC +10011	OH 26.5+0.6
1–0.....	43″	0.51	0.84	0.06
2–1.....	21	1.41	2.21	0.44
3–2.....	14	1.97	3.04	1.09
4–3.....	10	2.34	3.48	1.91
5–4.....	8.7	2.55	3.72	2.87
6–5.....	7.3	2.66	3.95	4.01

NOTES.—The predicted peak antenna temperatures calculated for a 15 m telescope working at its diffraction limits for each transition.

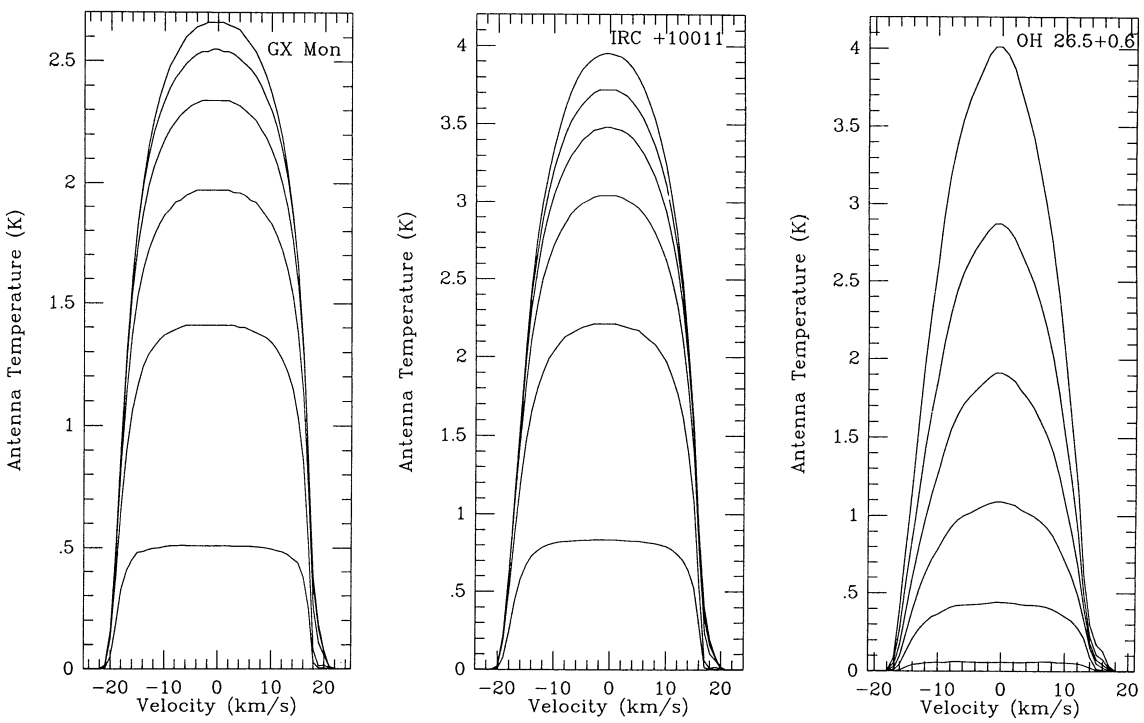

FIG. 6.—The predicted line profiles for the three stars under investigation from $J = 1$–0 to $J = 6$–5 transition for a telescope with a diameter of 15 m and a beamwidth at the diffraction limit for each transition.

history of mass loss from the stars. Also, the gas kinetic temperature of the envelope can be estimated and compared to the calculations. For our sample stars, it could be that for GX Mon, we see the star losing mass at a low rate, indicative of an early AGB phase; hence, we do not expect the mass-loss rate to vary from one region of the envelope to another by a large factor. For IRC +10011, the higher mass-loss rate could mean that it has undergone several thermal pulses, each resulting in an increase in the mass-loss rate if the stellar luminosity and the period increase (e.g., Wood 1990). In this case, we can expect a higher mass-loss rate near the star than in the outer envelope, which is seen when comparing the dust mass-loss rates from the infrared modeling and that obtained in this paper in order to fit the CO observation. This is illustrated more clearly in the case of OH 26.5+0.6, which may be in a superwind phase.

We also "map" the three stars using an arbitrarily large telescope in order to achieve a 1″ beam for all transitions up to $J = 6$–5. Resulting integrated line fluxes for each star as a function of offset from the source center are shown in Figure 7. Each transition has been normalized at 0″ offset, i.e., on source flux. It can be seen from the figure that as we move off the source, fluxes drop of very quickly. Table 4 shows the FWHM of three sources at all transitions. Higher transitions have smaller source sizes, as can be expected from the decreasing excitation temperature as a function of distance from the central star. OH 26.5+0.6 is barely resolved with the source size of less than 2″. Note that source sizes of all three objects are very small; hence, in order to map them, a very large telescope or an interferometer will be required.

TABLE 4

SOURCE SIZES

TRANSITION	SOURCE SIZE		
	GX Mon	IRC +10011	OH 26.5+0.6
1–0.....	4″.09	3″.81	1″.18
2–1.....	2.46	2.40	1.19
3–2.....	1.93	1.87	1.16
4–3.....	1.60	1.61	1.14
5–4.....	1.42	1.45	1.13
6–5.....	1.29	1.34	1.12

NOTES.—Source sizes as a function of offset in arcseconds for various transitions for the stars under investigation. Source size is defined as FWHM of the peak flux (see Fig. 7).

5. SUMMARY

We have attempted to calculate dust and gas mass-loss rates in a self-consistent way for O-rich stars, using results from Justtanont & Tielens (1992). In previous modeling attempts, the gas kinetic temperature was often taken to be a power law. Our models take into account the gas and dust temperatures as calculated from the heating and cooling in the envelopes and from mid-infrared modeling. We have chosen three stars with differing mass-loss rates in order to see how these affect the calculations.

From modeling CO rotational lines, it is clear that mass loss is not a static phenomenon. The results obtained from fitting the near- and mid-infrared spectra correspond to dust lying relatively close to the star. The CO mass-loss rates derived from the $J = 1$–0 and $J = 2$–1 transitions, however, measure the gas mass-loss rate in the outer part of the envelopes. For GX Mon, the predicted temperature in the $J = 2$–1 transition is higher compared to observations, when fitting the line profile for the $J = 1$–0 transition. This may be due to actual variation in the mass-loss rate. In the case of IRC +10011, the dust mass-loss rate derived by modeling the energy distribution (Justtanont & Tielens 1992) leads to too high CO $J = 1$–0 and 2–1 line fluxes. We have to reduce the dust mass-loss rate in order to fit the line profiles obtained from various observations. An even more extreme case is OH 26.5+0.6, which has a mass-loss rate estimated by infrared continuum model and the momentum equation of $5 \times 10^{-4}\ M_{\odot}\ \mathrm{yr}^{-1}$. The observations of this source show very low temperatures for both $J = 1$–0 and 2–1 transitions, which has been interpreted as indicating that the envelope has too low a temperature to even excite CO molecules into the first excitation state (Heske et al. 1990). However, we find that this explanation is untenable. In this paper, we tried modeling this source with a discontinuity in mass-loss rate in order to explain the low antenna temperature observed by Heske et al. (1990). Since the dust mass-loss rate is high, this leads to an extremely high gas mass-loss rate, assuming a radiation calculat dominated system. OH 26.5+0.6 is taken to be an extreme AGB star since it has a long pulsation

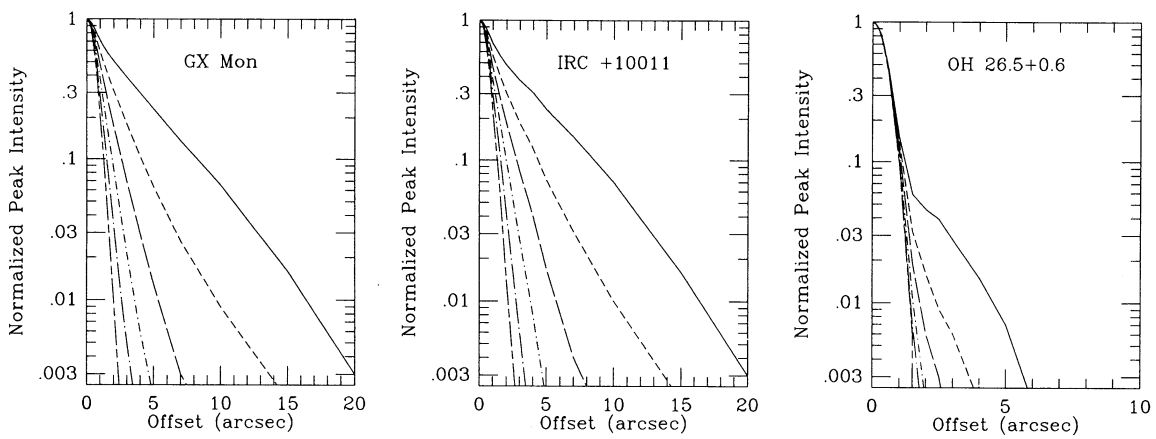

FIG. 7.—Normalized integrated line fluxes for $J = 1$–0 to $J = 6$–5 transitions for GX Mon, IRC +10011, and OH 26.5+0.6. Note that the higher the transition, the smaller the profile width. (*Solid line*) $J = 1$–0; (*short-dashed line*) $J = 2$–1; (*long-dashed line*) $J = 3$–2; (*short-dash-dot line*) $J = 4$–3; (*long-dash-dot line*) $J = 5$–4; (*long-dash short-dash line*) $J = 6$–5.

period of 1570 days (Suh, Jones, & Bowen 1990) and a very large dust optical depth. It is very likely that this source is in a superwind phase that lasts at most a few thousand years. There must have been a period when the star was losing mass at a more tenuous rate. By probing the outer part of the envelope, the enhanced mass loss due to the superwind is not yet being observed, and hence we are looking at the remnant of the red giant wind, which is much lower than estimated from the mid-infrared mass-loss rate.

In order to model these stars successfully, the code should take into account the variable mass-loss rates in the stellar lifetime. This is an ambitious project but may lead to a better understanding of mass loss and hence stellar evolution on the AGB.

REFERENCES

Anders, E., & Grevess, N. 1989, Geochim. Cosmochim. Acta, 53, 197
Bakes, E. L. O., & Tielens, A. G. G. M. 1994, ApJ, 427, 822
Bedijn, P. J. 1987, A&A, 186, 136
Bujarrabal, V. J., & Nguyen-Q-Rieu, 1981, A&A, 102, 65
Chackerian, C. 1976, J. Chem. Phys., 65, 4428
Flower, D. R., & Launay, J. M. 1985, MNRAS, 214, 271
Gilman, R. C. 1972, ApJ, 178, 423
Goldreich, P., & Scoville, N. 1976, ApJ, 205, 144
Hamann, W. R. 1981, A&A, 93, 353
Herbst, E., & Knudson, S. 1981, ApJ, 245, 529
Hempe, K., & Schonberg, K. 1986, A&A, 160, 141
Heske, A., Forveille, T., Omont, A., van der Veen, W. E. C. J., & Habing, H. J. 1990, A&A, 239, 173
Huber, K. P., & Herzberg, G. 1979, Molecules and Molecular Structure (Reinhold: van Nostrand)
Hyland, A. R., Beckwith, E. E., Frogel, J. A., & Neugebauer, G. 1972, A&A, 16, 204
Iben, I., Jr., & Renzini, A. 1983, ARA&A, 21, 271
Justtanont, K., & Tielens, A. G. G. M. 1992, ApJ, 389, 400
Kastner, J. H. 1992, ApJ, 401, 337
Knapp, G. R., & Morris, M. 1985, ApJ, 292, 640
Knapp, G. R., Phillips, T. G., Leighton, R. B., Lo, K. Y., Wannier, P. G., Wootten, H. A., & Huggins, P. J. 1982, ApJ, 252, 616
Letzelter, C., Eidelsberg, M., Rosatas, F., Breton, J., & Thieblemont, B. 1987, Chem. Phys., 114, 273
McKee, C. F., Storey, J. W. V., Watson, D. M., & Green, S. 1982, ApJ, 361, 673
Margulis, M., van Blerkom, D. J., Snell, R. L., & Kleinmann, S. G. 1990, ApJ, 361, 673
Mamon, G. A., Glassgold, A. E., & Huggins, P. J. 1988, ApJ, 328, 797
Mathis, J. S., Rumpl, W., & Norsieck, K. H. 1977, ApJ, 217, 425
Mihalas, D., Kunaz, P. B., & Hummer, D. G. 1975, ApJ, 202, 465
Morris, M. 1975, ApJ, 197, 603
Sahai, R. 1990, ApJ, 362, 652
Schatz, G. C., & Elgersma, H. 1980, Chem. Phys. Lett., 73, 21
Schonberg, K. 1985, A&A, 148, 405
Schonberg, K. 1988, A&A, 195, 198
Schonberg, K., & Hempe, K. 1986, A&A, 163, 151
Schutte, W., & Tielens, A. G. G. M. 1989, ApJ, 343, 369
Sopka, R. J., Olofsson, H., Johansson, L. E. B., Nguyen-Q-Rieu, & Zuckerman, B. 1989, A&A, 210, 78
Striker, J. 1978, J. Chem. Phys., 68, 934
Suh, K. W., Jones, T. J., & Bowen, G. H. 1990, ApJ, 358, 588
te Lintel Hekkert, P., Versteege-Hensel, H. A., Habing, H. J., & Wiertz, M. 1989, A&AS, 78, 399
Tielens, A. G. G. M. 1983, ApJ, 271, 702
Wattenbach, R., Krugel, E., Roser, H. P., Nett, H., Schwaab, G., & Densing, R. 1988, A&A, 202, 133
Wood, P. R. 1990, in From Miras to Planetary Nebulae: Which Path for Stellar Evolution? ed. M. O. Menessier & A. Omont (Paris: Editions Frontières)